

Quantitative determination of stress by inversion of speckle interferometer fringe patterns: experimental laboratory tests

Douglas R. Schmitt, Mamadou S. Diallo* and Frank Weichman

Institute for Geophysical Research, Department of Physics, University of Alberta, Edmonton, Alberta, T6G 2J1, Canada. E-mail: doug@phys.ualberta.ca

Accepted 2006 May 22. Received 2006 May 22; in original form 2006 March 11

SUMMARY

Quantitative determination of crustal stress states remains problematic; here we provide a synopsis of work that is leading towards the development of an optical interferometric method that may be applied in boreholes. The major obstacle to the continued development of this technique has been the problem of determining the state of stress within a stressed continuum; we demonstrate the solution of both the technical and analytical issues in this contribution. Specifically, dual beam digital electronic speckle interferometry is used to record the stress-relief displacements induced by the drilling of blind holes into blocks subject to uniaxial compressive stresses. Speckle interferograms are produced at rates near 4 Hz using a local Pearson's correlation method and are stored for analysis. This time-lapse capability is useful when transient effects, such as thermal expansion displacements produced by the heat of drilling or ongoing time-dependent deformation, are active. Four acrylic blocks subject to uniaxial compressions from 3.8 to 5.5 MPa with the compressions oriented at different angles with respect to the axes of the interferometry system were studied. Relative fringe phase information was extracted from appropriate interferograms and inverted to provide a quantitative measure of the 2-D stress field within the block. In general, the largest value of the stress obtained in the inversion agreed with the known stress to better than 70 per cent. These measurements suggest the levels of uncertainty that might be expected by use of such optical interferometric techniques. This technique may show promise for quantitative stress determination in the earth to complement existing techniques. As well, while the interferometric principles are not exactly the same as for the popular satellite-based INSAR techniques, the optical method here has the potential to be useful in analogue physical model laboratory studies of deformation in complex structures.

Key words: downhole logging, instrumentation, residual stress, rheology, stress distribution, thermal conductivity.

INTRODUCTION

The stress environment in rock controls the tectonic faulting regime, the initiation of seismic and aseismic displacement, and the propagation of fractures. Stress also influences the *in situ* values and anisotropies of seismic velocities, permeability, and electrical conductivity (e.g. Adams & Williamson 1923; Boness & Zoback 2004; Kaselow & Shapiro 2004). Knowledge of stress states is also necessary for safe and economic underground construction, resource extraction, and waste isolation using bore holes. Taken together there is a need for quantitative stress measurement in rock; however, the history of stress measurement in the earth is still relatively

new (Fairhurst 2003) and the quantitative determination of the stress tensor remains challenging. Numerous complementary techniques (Amadei & Stephansson 1997; Ljunggren *et al.* 2003) including hydraulic fracturing, overcoring, microseismic monitoring, borehole breakout and core-disk analysis and finite element modelling, are employed. Few of these provide the complete stress tensor; and there remains a need for ongoing innovation. Here we summarize progress towards the development of an optical interferometric stress-relief method that has the potential to provide the complete state of rock stress in the earth. This work builds on much earlier contributions (Bass *et al.* 1986) but with substantially improved recording technology and with much more mature understanding of the underlying problems.

Interferometric methods are finding increasing use in the geosciences. Satellite-based radar 'interferometry' (e.g. Massonnet & Feigl 1998) is able to provide measures of centimetre-scale displacements that occurred between two or more passes of a satellite. In

*Now at: ExxonMobil Upstream Research Company, Room URC-GW3-852A, PO Box 2189, Houston, TX 77252-2189, USA.

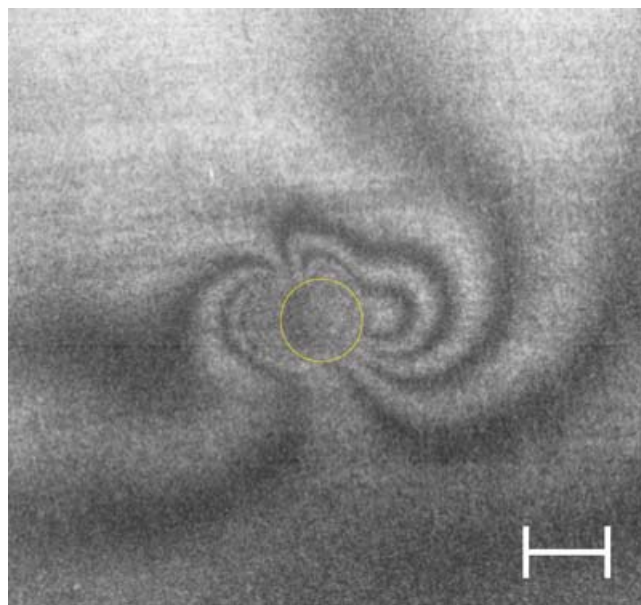


Figure 1. Example of a double exposure stress-relief hologram displaying a fringe pattern produced by stress-relief displacements induced by drilling a small (~ 1 cm diameter) hole perpendicularly into the borehole wall rock. From Schmitt (1987).

this method, fringe patterns are calculated essentially on the basis of the shifts in traveltimes of radar pulses scattered back from the same point on the Earth's surface to the satellite. The data may be displayed in terms of the phase variations as fringe patterns. This has numerous applications in monitoring earthquake motions, volcano inflation, petroleum or water reservoir depletion, slope stability, lake levels, and even localized building subsidence.

The applications of sensitive optical interferometric tools with micron-magnitude sensitivity in the earth sciences, however, remain limited. A short listing (Cloud 1995) of such image-based optical interferometric techniques includes double-exposure holographic interferometry, Moiré interferometry, and electronic or digital speckle interferometry (ESPI; DSPI). The details of these methods differ, but in general the final raw result is a 2-D fringe pattern superimposed on the surface of the object of study. For purposes of illustration only, an example of a film-based, double exposure hologram recording the stress-relief field acquired at one azimuth along a borehole drilled in a mine pillar is given in Fig. 1 (Schmitt 1987). The lobes of the fringes in this image results from micron-magnitude stress-relief displacements induced by drilling a small hole into the stressed wellbore wall rock; that such images may be obtained in the earth in these early studies continues to motivate the current ongoing research. For comparison, some more modern examples of raw fringe patterns obtained electronically during the course of the present laboratory tests are shown in Fig. 2.

There are few but notable contributions in which optical interferometry has contributed to problems in geophysics. Spetzler and coworkers (Spetzler *et al.* 1974, 1981) used holographic interferometry to monitor deformation on rock samples subject to uniaxial and polyaxial states of stress to failure. At low stress levels, the rocks displayed highly complex but uniform surface strain patterns. More significantly, prior to macroscopic fracture propagation, the eventual failure location displayed large and discontinuous deformation—perhaps the first observations of such localized phe-

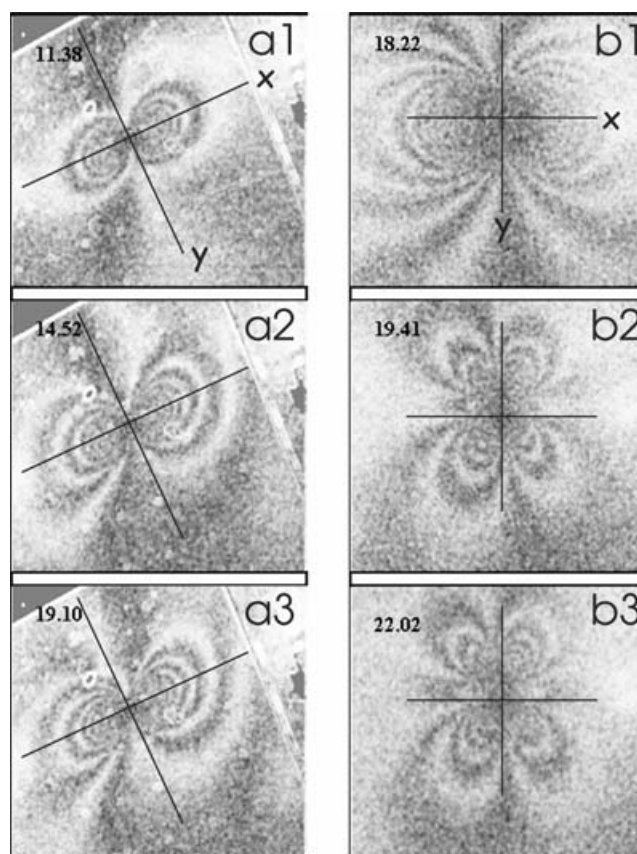


Figure 2. Examples of raw electronic speckle interferometry (ESPI) fringe patterns produced by stress-relief drilling calibration tests for different geometrical configuration and stress levels and illustrating time-dependent effects. Images have not been corrected for distortion due to the optical imaging geometry. The centre of the stress-relieving hole is at the intersection of the black lines. The sequence of interferograms in the left panel [a(1–3)] were obtained in the case where a uniaxial stress of approximately 4 MPa is applied along the X direction. The sequence in the right panels [b(1–3)] were acquired in the case where the applied stress of 5.4 MPa is along the Y direction. The file writing time from the computer clock in hours:minutes format is shown in each panel. Fig. 2a-1 was taken 30 min after drilling. Fig. 2b-1 was taken 1 min after drilling.

nomina in shear fractures. Takemoto (1989) has pioneered the use of interferometric methods as sensitive tunnel detectors of long period earth strains (Takemoto 1986; Takemoto *et al.* 2004) and tidal deformations (Takemoto 1990), and to determine stress (Mizutani & Takemoto 1989; Takemoto 1996). Other applications in the earth sciences have focused on the study of fracture processes (Maji & Wang 1992; Biolzi *et al.* 2001; Wang *et al.* 1990), determination of elastic properties (Schmitt *et al.* 1989; Park & Jung 1988) and, as already mentioned, stress determination from a borehole (Bass *et al.* 1986).

In contrast, the mechanical engineering, applied optics, metrology, and medical literature describe numerous optical interferometric techniques for measuring displacements, strains, stresses, fracture growth, and inelastic deformations of a wide variety of materials and structures. Some advantages of optical techniques over more conventional methods, such those employing strain gages, are that deformation over a large area is observed, that the object of study is not disturbed by the measurement system, and that minimal sample preparation is necessary. Further, analysis of strain gage results are complicated because they do not provide a point

measurements and the integration of the deformation within the bounds of their finite surface area must be accounted for. Early work was primarily restricted to qualitative mapping of deformations via discontinuities in the raw observed fringe patterns useful in detecting defects. Currently, ready access to inexpensive lasers, digital image acquisition hardware, and image processing software allows such techniques to be employed for an ever wider variety of applications.

As noted, this issue of determining the state of stress in the Earth's crust is an essential consideration in many geotechnical and geophysical problems (e.g. Amadei & Stephannson 1997). In mechanical engineering fields too, processes very often involve localized heating, differential thermal expansion, or deformation that create an internal (residual) stress which may be retained in the finished component. Determining these residual stresses is essential for the safety assessment and lifetime of the machined component. In short, there are numerous needs for accurate quantitative measurements of the stress tensor, both applied and residual, and while a number of complementary techniques exist, achieving this goal remains challenging (Whiters & Badheshia 2001; Engeldger 1993) particularly if quantitative information on *in situ* stress magnitudes and directions are required.

In mechanical engineering, literature revolves around the blind-hole drilling technique that is widely used to measure potentially destructive residual stresses induced in a piece during its fabrication, and there has been some tests of the blind-hole drilling concept for stress measurement within the earth. (Smither *et al.* 1989). In this technique, a small hole is drilled in the sample creating a stress-free boundary that induces local stress-relief displacement of the sample's surface (Fig. 3). These displacements depend on numerous factors such as the magnitudes of the applied stresses, the hole radius a and depth h , and the elastic properties of the medium in which the hole is drilled. The displacement field can further be complicated by 3-D stress gradients within the material. The state of stress may be determined from these displacements or strains using an appropriate model of the stress-relief displacements based on linear elasticity theory or empirical analyses. The development of appropriate stress-relief displacement models in three dimensions now allows better use of the interferometric techniques.

In this study, ESPI is used to record stress-relief displacements induced by the drilling of blind holes into pre-stressed materials.

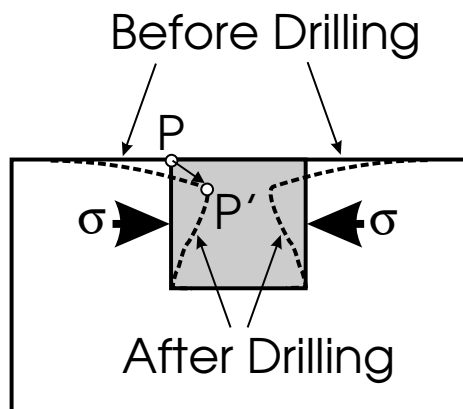


Figure 3. Exaggerated view of drilling-induced stress relief displacements into a half-space. Point P on the surface is displaced to P' after drilling; grey-fill area represents the blind hole. In reality, the hole diameters and depths will be in the millimetre to centimetre range while the stress-relief displacements are on the order of a few micrometres.

The experiment is conducted for different stress levels and for different geometrical configurations of the optical system with respect to the uniaxial stress direction acting on the specimen. Observed fringe patterns are inverted using an iterative least squares minimization approach that uses the positions of fringes minima and maxima to determine the magnitude of the applied stress. The results in this paper are achieved because a number of technical and analytical problems were solved. These problems, synoptically reviewed here, retarded the use of optical methods for quantitative stress determinations. Although the current work was carried out in a polymer, this step is necessary in order to validate the technique itself even though the final goal is to achieve a method that may be applied to stress measurement from boreholes. The paper concludes with a discussion of where this method might best be applied in the context of stress and deformation measurement in the geosciences.

BACKGROUND

Relief-based stress determinations, of which overcoring is perhaps the best known example in the geosciences, require:

- (1) knowledge of the relationship between the stress-relief induced deformations and the *in situ* stress field,
- (2) a method to adequately record such a deformation and
- (3) the ability to invert observed deformations to obtain values of the stress field.

Recent developments in each of these three components of the stress-determination problem are reviewed here briefly in order to prepare the reader for a presentation of the final experiments.

Stress-relief displacement field

This section focuses solely on the isolated problem of determining a biaxial state of stress within a plate. The connected problem which uses the concepts developed here in obtaining the complete state of stress from a borehole is reviewed later.

The essential concept behind stress-relief stress measurement techniques are that changing the geometry of an object by, for example, drilling a small hole into its surface necessitates a redistribution of the stresses within the object. This redistribution is manifest in small changes to the shape of the object that will be dependent on the magnitude of the stresses in question (Fig. 3). Hence, the induced deformations can in principle directly provide information on the stresses.

By the 2-D symmetry of the hole in the plane of the surface of the object, workers initially developed straightforward plane strain expressions for use in the analysis of strain gage readings. These formulae were based on the plane strains expected in the vicinity of a through-going hole in a thin plate (Fig. 4a) subject to a state of 2-D plane stress with principal stresses σ_{\max} and σ_{\min} of the form:

$$\varepsilon(r, \chi) = A(\sigma_{\max} + \sigma_{\min}) + B(\sigma_{\max} - \sigma_{\min}) \cos(2\chi), \quad (1)$$

where ε can be either the radial or the azimuthal strain and χ is the azimuthal angle as measured from the direction of σ_{\max} . A and B are factors that depend on the stress-relieving hole radius a , the distance from the hole axis r , and any two of the independent elastic properties such as Young's modulus E and Poisson's ratio ν . Examination of eq. (1) highlights the $\cos(2\chi)$ behaviour of the strains around the hole. This is most simply illustrated in the formulae for the factors

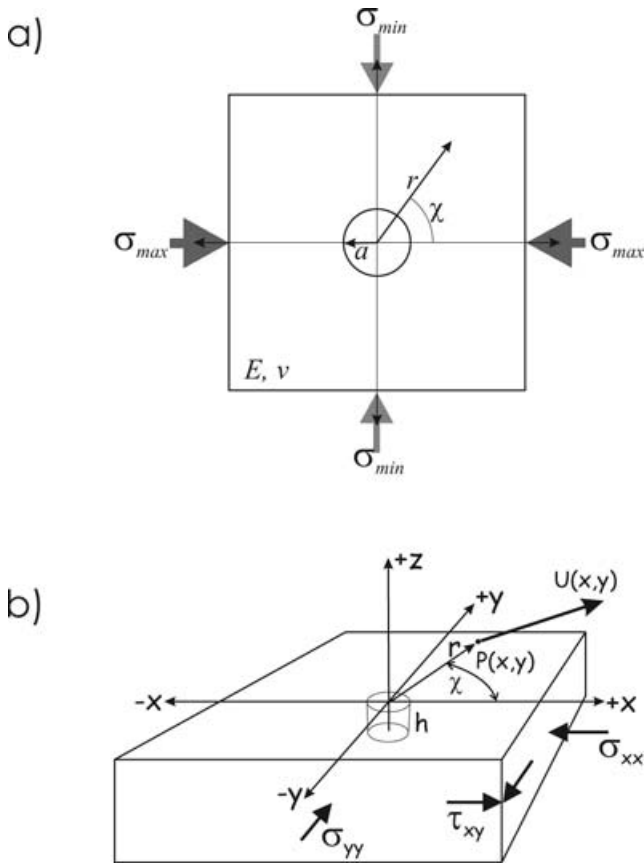


Figure 4. (a) Plan view of plate or block surface with coordinate systems employed. (b) Geometry of the stress-relief hole in an object subjected to a state of plane stress relative to Cartesian coordinates (x, y, z) and cylindrical (r, χ, θ) coordinate system. Hole axis coincides with the z -axis. The object is assumed to be subject to a 2-D state of plane stress with normal components σ_{xx} , σ_{yy} and shear component τ_{xy} .

for the case of plane stress within a thin sheet with a through-going hole with:

$$A = -\frac{1+\nu}{2E} \left(\frac{a}{r} \right)^2, \quad (2)$$

$$B = -\frac{1+\nu}{2E} \left[\frac{4}{1+\nu} \left(\frac{a}{r} \right)^2 - 3 \left(\frac{a}{r} \right)^4 \right]$$

Similar $\cos(2\chi)$ -based formulae can be written for the particle displacements instead of the strains; the optical method employed here is directly sensitive to the actual stress-relief displacements of the surface.

In trying to measure stress in the earth, however, the case actually encountered is not that of a thin plate but of a stressed half-space in which a blind (i.e. finite depth) stress-relieving hole is drilled (Fig. 4b). In this situation, all three components of the surface stress-relief displacement field $\mathbf{U}(x, y) = u_x(x, y)\mathbf{i}_x + u_y(x, y)\mathbf{i}_y + u_z(x, y)\mathbf{i}_z$ (Fig. 4b) induced for all points $P(x, y)$ over the surface of the object (Fig. 5a) may need to be considered. Unfortunately, obtaining a representative relationship between the stresses and the induced displacements is not straightforward (see Schmitt & Li 1996, for a review), and this causes difficulties even in the commonly applied strain gage measurements that record only the two strains in the plane of the surface. The 3-D asymmetry of the blind hole makes construction of a purely analytic solution from first principles awk-

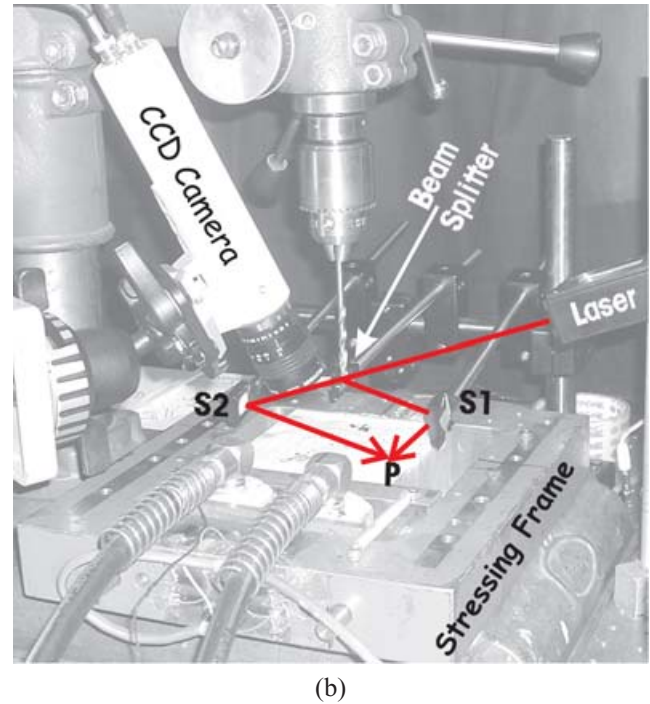
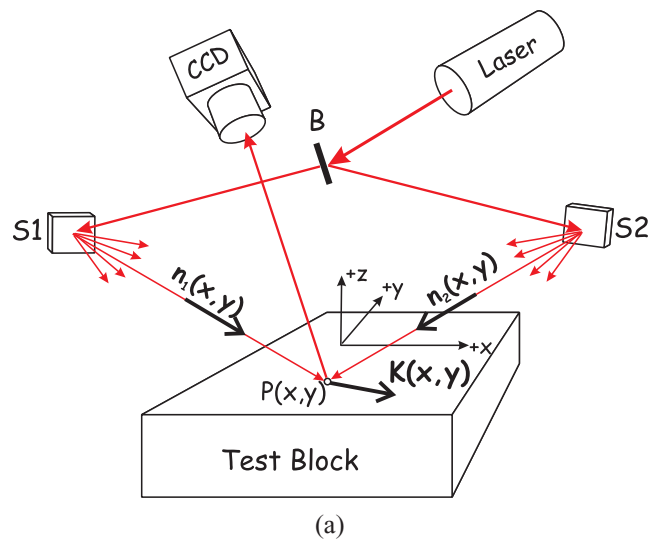


Figure 5. (a) Experimental geometry with the laser beam split at B , and $S1$ and $S2$ the source points with unit wavenumber direction vectors $\mathbf{n}_1(x, y)$ and $\mathbf{n}_2(x, y)$, respectively. $P(x, y)$ is one point on the surface of the object, and $\mathbf{K}(x, y) = \mathbf{n}_1(x, y) - \mathbf{n}_2(x, y)$ is the sensitivity vector for P . (b) Photograph of experimental set-up with beam paths to a point $P(x, y)$ shown.

ward. Early engineering practice navigated around this problem with carefully controlled calibration testing for determination of appropriate values for the factors A and B (Rendler & Vigness 1966) that depend on the ratio of the hole depth h to its radius a .

A drawback of this approach is that its utility is limited to the particular geometry studied; and to overcome this limitation numerical finite element calculations have provided supplementary information upon which current engineering standards are based (Schajer 1981). Numerical methods have also been used in studying stress-relief problems in engineering (Nelson & McCrickerd 1986; Beghini & Bertini 2000; Furguele *et al.* 1991), but for the most part these

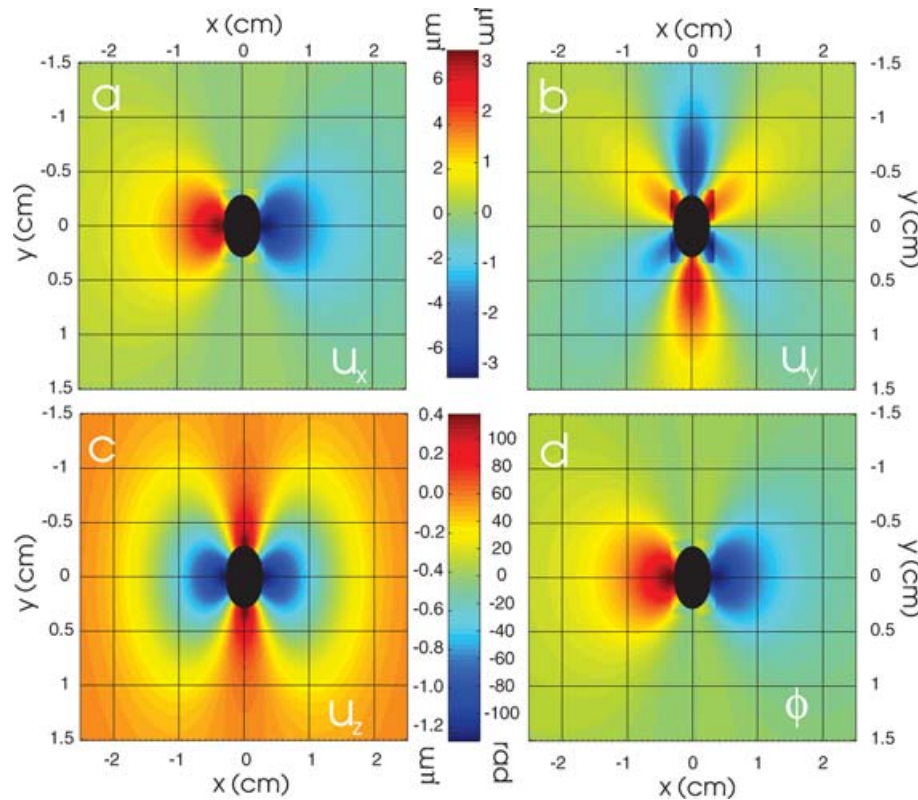


Figure 6. Calculated elastic stress-relief displacement components produced by drilling a blind hole ($a = 3.426$ mm, $h = 1.36$ cm, $E = 3$ GPa, $\nu = 0.4$) (a) $u_x(x, y)$, (b) $u_y(x, y)$, and (c) $u_z(x, y)$ (colourbar axes correspond to μm) that will produce (d) a phase map (colourbar axis correspond to phase angle ϕ in radians) using the same geometry of Test 1 in Table 1. Grid spacing in terms of cm centred at **O**. Note that x and y axes are not to the same scale in order to better compare to real distorted fringe patterns.

calculations were still carried out on a case-by-case basis dependent on the particular problem.

To overcome these difficulties, Ponslet & Steinzig (2003) more recently developed sets of look-up interpolation tables that may be used to describe the stress-relief displacements for holes with $0.2 \leq h/a \leq 1.4$ that are drilled into materials with $\nu = 0.3$ (i.e. typical of many aluminium and steel alloys of interest in mechanical engineering). By curve fitting the results from an extensive series of finite element cases, Rumzan & Schmitt (2003) independently constructed a series of parametric equations that describe the 3-D stress-relief displacement field. These formulae are generally valid for hole depth/diameter ratios from 0.5 to 4.0, for Poisson's ratios from $0.05 \leq \nu \leq 0.45$, and over radial distances from the hole axis from 2 to 20 times the hole radius, although these validity ranges can vary with hole depth. These parametric formulae are too lengthy to be reproduced here, but typical maps of the stress-relief displacement fields are found in Fig. 6. The greater range of Poisson's ratios allows application of the methods to ceramics, rocks, and polymers that do not necessarily have $\nu \sim 0.3$. It is important to note that the 'shape' of the displacement field is controlled primarily by ν and the ratio h/a of the hole depth to its radius. The ratio between the stresses and Young's modulus E control only the magnitudes of the displacements; and consequently, the use of E and ν in describing the material's elastic properties is advantageous over other combinations of the elastic moduli.

It is useful to point out that in machined or welded metallic objects, the gradients in the residual stress near the surface can be large (on the order 100 MPa mm^{-1}), which can lead to failure of the material. This problem is not as severe in earth science contexts

and the present work assumes that a uniform biaxial state of plane stress exists in the object prior to drilling the stress-relieving hole.

For a single uniaxial stress, this parametrization allows one to describe a stress-relief displacement field as a series of vector basis functions $\mathbf{u}(x, y, \nu, h/a)$ containing the field shape such that the expected true stress-relief deformations can be found via $\mathbf{U}(x, y) = (\sigma_{yy}/E)\mathbf{u}$. This uniaxial basis is readily rotated to provide solutions for the two remaining stress components σ_{xx} and τ_{xy} using well-known 2-D stress-rotation formulae. At a given point (x, y) on the surface, these basis functions may be combined in a displacement field shape matrix $S(x, y)$:

$$S(x, y) = \begin{bmatrix} u_x^{xx} & u_x^{yy} & u_x^{xy} \\ u_y^{xx} & u_y^{yy} & u_y^{xy} \\ u_z^{xx} & u_z^{yy} & u_z^{xy} \end{bmatrix}, \quad (3)$$

where u_x^{xy} for example is the x-component basis displacement induced by the shear stress τ_{xy} . If the simple case of biaxial stress (Fig. 4) is allowed to be represented as a column vector $\sigma = [\sigma_{xx}, \sigma_{yy}, \tau_{xy}]$, then the displacement at a given point in compact matrix form is $\mathbf{U}(x, y) = S(x, y) \sigma$. An example of the u_x , u_y , and u_z displacements for a representative case of a block subject to an uniaxial σ_{xx} stress illustrates the complex 3-D pattern described by $S(x, y)$ (Fig. 6).

Electronic speckle interferometry

As noted earlier, the stress-relief displacements induced by the drilling of a small, blind hole into manufactured objects have long

been studied as a means of estimating possibly deleterious residual stresses in machined objects. Standardized strain gage techniques (see ASTM 2001) to do this have long predominated. Some disadvantages of strain gages, however, are that they must carefully be glued to a specially prepared surface with a high degree of precision in positioning, that their calibration carries a degree of uncertainty, and that they provide only a measure of the average strain over their areal extent. This last point is particularly important given the rather large strain gradients near the stress-relieving hole. Strain gages have been directly applied to rock for stress determination also, but issues of access down long wellbores, surface roughness, and moisture complicate such procedures. This provides an opportunity for optical methods, which often do not require any direct contact between the recording system and the rock mass and which can provide full field measurements over the surface of the object as shown in Fig. 2.

Traditionally, the stress-relief strains in the vicinity of the drilled hole are measured using specialized strain gage rosettes (see ASTM 2001). However, optical techniques such as Moiré interferometry (McDonach *et al.* 1983; Schwarz *et al.* 2000) holographic interferometry (Makino *et al.* 1996; Bass *et al.* 1986) and DSPI or ESPI, respectively, (Jones & Wykes 1989; Vikram *et al.* 1995; Zhang 1998; Schmitt & Hunt 1999; Diaz *et al.* 2001) have been used in various fields to provide quantitative information about the displacement field generated by the drilling operation. The data analysis is based on comparing the interference field before and after drilling operation.

Speckle interferometry is employed in this study. The roughness of the surface scatters the coherent laser light such that it interferes

to form small dark and bright areas that can be seen over its surface, this granular appearance of objects seen under laser light is called speckle. The granular speckle pattern may then be captured using readily available CCD (charge-coupled device) cameras and stored as a bit-mapped grey-scale image (Figs 7a and b). By itself, this speckle pattern contains little useful information. However, an interesting aspect of these speckles is that when illuminated under crossed coherent beams, each speckle essentially acts as an independent interferometer. If the beams remain stationary but the surface of the object is displaced, the speckle's intensity will harmonically cycle from dark to bright. Speckle interferometry requires the speckle patterns of the object surface be obtained both before and after the deformations occur.

In practice, a laser beam is divided by a splitter into two secondary beams that are redirected to illuminate and interfere on the surface of the specimen (Fig. 5). When used with blind-hole drilling, images stored before (Fig. 7a) and after (Fig. 7b) the drilling operation are compared either by intensity subtraction or local cross-correlation. The resulting image (Fig. 7c) exhibits a fringe pattern that is a map of the changes in the phase of the light due to displacements of the surface. The shape and spacing of successive fringes depend on the magnitude and direction of surface displacement due to external or residual stresses and on the geometry of the optical set-up. The fringe pattern is really an (x, y) map of the changes in the phase of the light due to displacements of the surface according to:

$$\begin{aligned}\phi(x, y) &= \mathbf{K}(x, y) \cdot \mathbf{U}(x, y) \\ &= \frac{2\pi}{\lambda} (\mathbf{n}_1(x, y) - \mathbf{n}_2(x, y)) \cdot \mathbf{U}(x, y)\end{aligned}\quad (4)$$

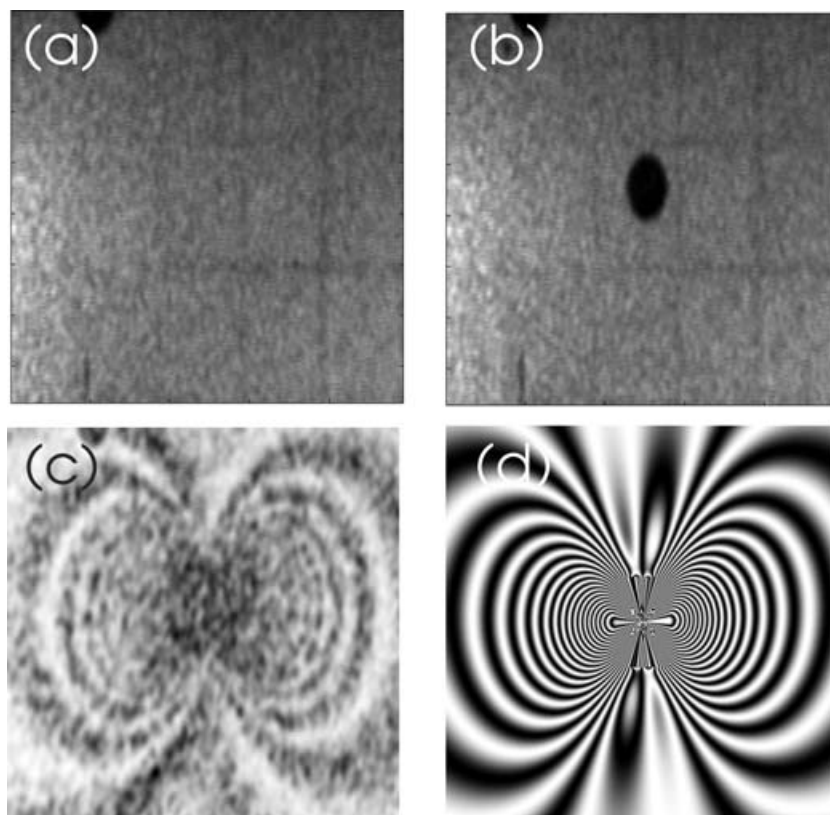


Figure 7. Raw speckle patterns recorded (a) before and (b) after stress-relief drilling. These are used to calculate (c) $\rho(x, y)$ fringe pattern, which is the observed data. This fringe pattern correlates to an unwrapped phase $\phi(x, y)$ map of Fig. 6 that may be used to calculate (d) the corresponding modelled fringe patterns.

where $\mathbf{U}(x, y)$ is the previously described vector describing the 3-D displacement of the surface at point $P(x, y)$, λ is the wavelength of the coherent light employed and, \mathbf{n}_1 and \mathbf{n}_2 are unit directional vectors that describe the light rays connecting $P(x, y)$ to the illumination source points $S1$ and $S2$, respectively (Fig. 5a). The vector $\mathbf{K}(x, y) = (\mathbf{n}_1 - \mathbf{n}_2)$ is called the sensitivity vector and it is a useful concept in that the final fringe pattern will be sensitive only to the components of $\mathbf{U}(x, y)$ projected along the direction of $\mathbf{K}(x, y)$. These fringe patterns serve as the raw data that is then analysed to provide measures of stress or particle displacement. For purposes of illustration, the set example set of displacements (Figs 6a–c) are mapped to $\phi(x, y)$ (Fig. 6d).

If $\phi(x, y)$ is an even integral multiple of π , the speckle will have the same intensity before and after a small displacement. In contrast, if $\phi(x, y)$ changes by an odd integral multiple of π , the intensity of the speckle will be different. The intensity of the speckle (or a small set of neighbouring speckles) experiencing odd or even multiple shifts of π will then correlate highly or not at all, respectively, before and after the deformation. A measure of the degree of correlation $\rho(x, y)$ is given by:

$$\rho(x, y) = (1 + \cos(\phi(x, y)))/2, \quad (5)$$

which varies between $0 \leq \rho(x, y) \leq 1$. A value of 1 means perfect correlation while values near zero indicate no correlation. Fig. 7(d) shows a theoretical fringe pattern obtained from the phase map of Fig. 6 and corresponds to the observed fringe pattern of Fig. 7(c). A variety of methods are employed to calculate the fringes (Vikram *et al.* 1995) controlled phase shifting. We use an alternate technique (Schmitt & Hunt 1997) that employs calculation of the Pearson's correlation coefficient between a number of local speckle intensities (Fig. 7c). This local correlation technique has the advantage that the calculated correlation coefficient can be directly compared to $\rho(x, y)$ in eq. (2) as well being applicable under conditions of non-uniform illumination over the surface of the object.

Inversion of fringe patterns for stress state

For convenience, it is useful to define the fringe order $N(x, y)$:

$$N(x, y) = \frac{\phi(x, y)}{2\pi}. \quad (6)$$

An integer value of N will correspond to perfect correlation and a 'bright' fringe in the final fringe pattern, while a value of an integer plus $\frac{1}{2}$ is the peak of a 'dark' fringe. N can take any real value, both negative and positive. This leads to one further aspect of the fringe patterns that is important. The fringe patterns themselves via eq. (2) can at best yield a wrapped phase map modulo π . That is, neither the true magnitude of $\phi(x, y)$ nor of $N(x, y)$ can be directly known from the calculated fringe pattern; obtaining this information requires that the true phase be found via phase unwrapping. Reviews of phase unwrapping techniques may be found in (Ghiglia & Pritt 1998) and are beyond the scope of this article. A complete phase unwrapping was not used here; rather a simpler method that requires picking the fringes was employed as a part of the inversion procedure.

The inversion procedure assumes that the stress-relief displacements are correctly described by the parametric model relating displacements to stress for the blind hole as are reviewed above. Combining eqs (1), (2) and (4) gives

$$N(x, y) = [K(x, y) \cdot S(x, y)]\sigma = g(x, y)\sigma, \quad (7)$$

where the row matrix $g(x, y) = [g^{xx} g^{yy} g^{xy}]$ is a condensation of the presumed 'knowns' of the experimental geometry (i.e. the positioning of $S1$ and $S2$ relative to $P(x, y)$) and the predetermined stress shape basis functions). A fringe pattern may easily be forward modelled using eqs (5) and (3) for a known stress state σ explicitly via:

$$\begin{bmatrix} N(x_1, y_1) \\ N(x_2, y_2) \\ \vdots \\ N(x_i, y_i) \\ N(x_{i+1}, y_{i+1}) \\ N(x_{i+2}, y_{i+2}) \\ \vdots \\ N(x_m, y_m) \end{bmatrix} = \begin{bmatrix} g^{xx}(x_1, y_1) & g^{yy}(x_1, y_1) & g^{xy}(x_1, y_1) \\ g^{xx}(x_2, y_2) & g^{yy}(x_2, y_2) & g^{xy}(x_2, y_2) \\ \vdots & \vdots & \vdots \\ g^{xx}(x_i, y_i) & g^{yy}(x_i, y_i) & g^{xy}(x_i, y_i) \\ g^{xx}(x_{i+1}, y_{i+1}) & g^{yy}(x_{i+1}, y_{i+1}) & g^{xy}(x_{i+1}, y_{i+1}) \\ g^{xx}(x_{i+2}, y_{i+2}) & g^{yy}(x_{i+2}, y_{i+2}) & g^{xy}(x_{i+2}, y_{i+2}) \\ \vdots & \vdots & \vdots \\ g^{xx}(x_m, y_m) & g^{yy}(x_m, y_m) & g^{xy}(x_m, y_m) \end{bmatrix} \begin{bmatrix} \sigma_{xx} \\ \sigma_{yy} \\ \tau_{xy} \end{bmatrix} \quad (8)$$

where m is the total number of points calculated. Eq. (6) may be condensed as $N = G\sigma$.

This forms the basis of the inversion algorithm for σ using observed values of N from numerous points in the fringe pattern over the surface of the object using the least squares formulation:

$$\sigma = (G^T G)^{-1} G^T N. \quad (9)$$

It is worthwhile noting that eq. (6) can be further adapted if necessary to include additional motions, such as a rigid body translation of the object itself, that superpose with the stress-relief displacements.

Although eq. (7) is straightforward to employ, it is more difficult to implement in practice because the fringe patterns are a wrapped phase representation and do not yield directly the value of $N(x, y)$ or, equivalently, $\phi(x, y)$. The problem is overcome here following an iterative procedure, (Schmitt & Hunt 2000) in which:

(1) Loci of constant fringe order, such as a continuous bright peak or dark trough, are picked manually from the image of the fringe pattern. Information on which points share the same fringe order and which other points are along an adjacent phase loci are noted (Fig. 8).

(2) A value of the fringe order is arbitrarily assigned to one of the loci and the neighbouring loci will be appropriately incremented or decremented. For example, a bright fringe must be assigned an integer value, say let $N = 1$. With this assignation, the adjacent dark fringe troughs must have respective fringe orders of $N = \frac{1}{2}$ and $1\frac{1}{2}$. Continuing this procedure values of $N = 0$ and $N = 2$ must then be assigned to the next adjacent sets of bright peaks on either side of the initial $N = 1$ fringe. This procedure is continued until all the picked fringes have fringe orders applied.

(3) The relative differences in the fringe order will be correct but the initial value of $N = 1$ may only be a guess, so the initial fringe order values are likely incorrect. Despite this, an inversion using these fringe orders in eq. (7) may be calculated to provide an estimate of σ that will have an associated error ε

$$\varepsilon = |N - G\sigma|^2. \quad (10)$$

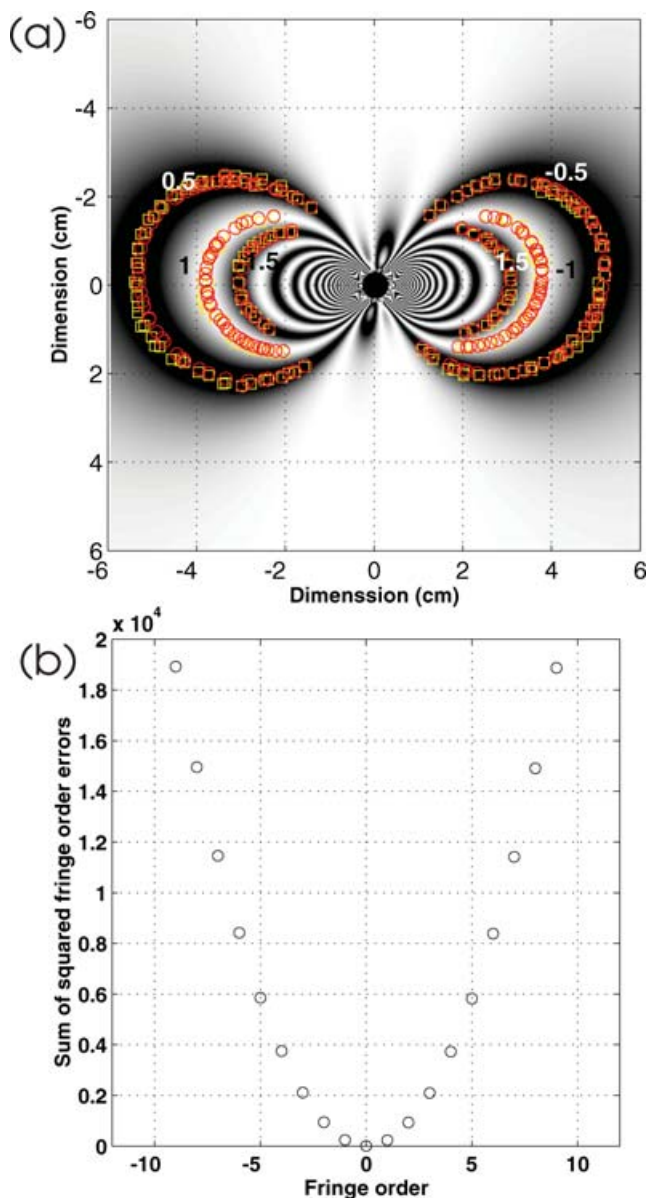


Figure 8. Illustration of the inversion procedure on the calculated fringe pattern. (a) Calculated fringe pattern for a uniaxial stress of $\sigma_{xx} = 5$ MPa applied to a block of material with $E = 3.1$ and $\nu = 0.3$ with a hole diameter of $4.50 < a < 5.71$ mm and $2.4 < h/a < 3.7$. Picked fringe points and initial fringe order assignments shown. (b) Evolution of the error ε versus fringe order assigned to the true $N = 0$ fringe.

(4) The fringe orders can then be updated by shifting the values by ± 1 and applying step 3 again to calculate a new value of the error.

(5) Step 4 is repeated until a satisfactory minimum value of the error ε is detected whereupon the best estimate of σ in the least squares sense will have been found. (Fig. 8b).

The example of Fig. 8 is purely hypothetical and it is instructive to see how well the inversion procedure involving the manual fringe picking works on noise-free synthetic fringe patterns. A number of such numerical tests were carried out. Fig. 8 shows $\sigma = [5 \ 0 \ 0]$ MPa. Direct inversion of the forward modelled results yields insignificant numerical error. Manual picking of the fringe peaks and trough and inversion according to the above protocol, however, yielded values

of $\sigma^1 = [5.006 \text{ MPa}, 90 \text{ kPa}, 0.6 \text{ kPa}]$. A second case with a different uniaxial applied stress aligned in the y direction ($\sigma = [0 \ 10 \ 0]$ MPa) yielded $\sigma^2 = [0.24 \ 9.3 \ 0.02]$ MPa upon inversion. A discussion of the source of these errors may be found in Shareef & Schmitt (2004).

Determination of the complete stress tensor from a borehole

Although the focus of this contribution is on obtaining the 2-D biaxial stress state in a plate, the ultimate goal is to find the 3-D rock stress in the earth from measurements in a borehole. This problem has been discussed earlier (Bass *et al.* 1986), but it is important to provide a brief review in order to place the current study in context.

It is first necessary to consider the concentration of stress by the borehole. Hiramatsu & Oka (1962) developed the equations for stress concentration by a wellbore drilled at an arbitrary angle relative to the three principal stresses existing in the linearly elastic continuum. One of their essential results is that a state of biaxial stress exists within the rock at the borehole wall, and this stress state consists of the azimuthal σ_θ and axial σ_z normal stresses and their associated shear stress $\tau_{\theta z}$. This stress state is a consequence of the concentration of the 3-D stress state that existed prior to drilling the borehole; and at a given depth will vary with azimuth. As noted, the method described here is only able to obtain the 2-D biaxial stresses at a given point. Consequently, determination of the pre-existing complete state of stress requires the 2-D biaxial stresses at a minimum of three azimuths in order to adequately solve for the six unknown components of the full 3-D tensor.

EXPERIMENTAL CONFIGURATION

The experiments here consisted of carrying out the hole drilling measurements on blocks subject to a uniaxial compressive stress. The experimental configuration (Fig. 5b) follows the ESPI geometry (Fig. 5a) closely. Interferometric techniques are particularly susceptible to contamination by vibration. To maintain stability as much as possible, the entire experiment is conducted on an air isolated optical bench. In our earlier studies (e.g. Schmitt 1987) we found that measurements within a borehole are also highly stable with regards to vibrations despite the fact that the measurements were carried out in an active mine. The beam from a 36 mW (Micro Laser Systems Model L4 830S) stabilized infrared diode laser ($\lambda = 830$ nm) is split by a 50:50 partially transparent beam splitter.

The two arms of the split beam strike and are scattered from the source points $S1$ and $S2$ (Table 1). Most workers employ systems of lenses to both collimate and expand their beams to illuminate the surface of the object. The present experiment uses a more novel approach in which the beams are expanded by scattering from an optically-rough, ground ceramic surface at $S1$ and $S2$. While this procedure may lead to some loss of light, it has a number of advantages in that the true coordinate positions of $S1$ and $S2$ within the chosen coordinate frame are easily measured, and that a nearly spherical expansion is effected producing a wide range of directions for the sensitivity vector $\mathbf{K}(x, y)$ allowing for better use of the fringe pattern data. On a more practical note, the entire system takes up less space and there is no requirement to keep lenses dust-free.

An infrared sensitive CCD camera (TI Multicam CCD) with a 8 mm f1.4 lens acquired the raw speckle patterns. It is worthwhile noting that a further advantage of the ESPI system is that, in principal, the placement of the camera is not important because $\mathbf{K}(x, y)$ depends only the positions of $S1$ and $S2$. The 24 bit grey-scale

Table 1. Experimental geometry and results.

Sample	Test 1 Ctest3	Test 2 Csp14	Test 3 b2f	Test 4 B3f
S1 Coordinates (cm)				
Ox	-9.102	-9.004	6.256	6.256
Oy	-3.792	-3.713	1.411	1.411
Oz	4.261	3.886	2.500	2.500
S2 Coordinates (cm)				
Ox	5.930	7.996	-8.793	-8.793
Oy	4.325	-4.620	-9.250	-9.250
Oz	4.606	4.405	2.700	2.700
Known applied stress (MPa)				
σ_{xx}	5.5	4.06	0	0
σ_{yy}	0	0	3.8	5.4
τ_{xy}	0	0	0	0
Inverted stress MPa				
σ_{xx}	5.30 (3.6 per cent)	4.67 (+15 per cent)	0.76	2.40
σ_{yy}	2.61	1.16	2.41(37 per cent)	5.20 (3.7 per cent)
τ_{xy}	1.48	0.85	0.12	0.97

image (640×480 pixel) is downloaded to a personal computer (*ca.* 2002) that employs a specialized interactive software (Engler 2002) that allows the fringe patterns to be calculated using the algorithm of Schmitt & Hunt (1997), and viewed in near real time (at four fringe patterns per second). Both the calculated fringe patterns and the raw speckle images are stored for later use; as suggested by the frames in Fig. 2, the ability to store many images is useful as it aids in the detection of potentially deleterious time-dependent effects.

The images of the block and fringe patterns in Fig. 2 are distorted due to the oblique placement of the recording camera relative to the stressing frame. In order to be able to correctly analyse the fringe patterns, the (x, y) location of each image pixel must be known. The mapping registration function was determined by taking an image of the object overlain with a fine grid paper aligned with known positions on the block.

The fringe patterns retain a degree of high spatial frequency speckle noise inherent in the method (Engler 2002). This noise makes delineation of the lower spatial frequency fringes difficult and adds error to the picking the bright and dark fringe loci for later analysis (Fig. 9). Many standard image processing smoothing functions (e.g. Fourier transform or median filtering) do not adequately remove the speckle noise and, indeed, can make the problem worse. Instead, we employed an alternative technique referred to as *mean curvature diffusion*. The details of this method (Diallo & Schmitt 2004) are beyond the scope of this paper but essentially the method uses an iterative procedure analogous to diffusion to remove the high-frequency noise, leaving the useful information of the fringes (Fig. 9). To illustrate the procedure, speckle is added to a hypothetical noise-free fringe pattern (Fig. 9a). Repeated application of the algorithm to the noisy fringes (Fig. 9b) better highlights the desired fringes (Figs 9c–e). A line plot of the image grey-scale values through the centre of the image (Fig. 9f) more quantitatively illustrates the improvement to the image with successive iterations although one disadvantage is the loss of some relative amplitude for the higher density fringes near the edge of the image.

The samples for these tests are acrylic (PMMA) blocks machined to dimensions of $12 \times 12 \times 5$ cm. Acrylic was selected for these calibration tests because it is homogeneous and isotropic and has a low Young's modulus of $E = 3.0 \pm 0.1$ GPa that allows sufficient stress-relief displacements under modest applied stresses below 6 MPa.

Both E and $\nu = 0.38 \pm 0.01$ were determined from samples taken from the blocks using standard strain gage methods on a universal testing machine, and this was further confirmed by a complementary interferometric method at similar induced displacement levels (Shareef & Schmitt 2004). After the initial machining the blocks are annealed at low temperature to eliminate the possibility of residual stresses in the material that would complicate the stress-relief pattern. This was checked by examining the samples for photoelastic birefringent fringes none of which were seen. The front surface of the block was then lightly 'pebbled' with white paint to ensure the light would be scattered from its surface. These blocks were then placed into a stressing frame whose applied force was measured using strategically placed strain gages in an unbalanced Wheatstone bridge arrangement that was frequently calibrated with a load cell. The block was subject to a known uniaxial stress that was carefully monitored for changes for a period of at least one day before making the actual stress-relief measurements. Four different stress states were tested (Table 1).

After being satisfied that the stress conditions on the sample were stable, a reference speckle image was taken prior to drilling. A 4.5 or a 4.71 mm diameter hole was drilled to 15 mm in depth, depending upon the bit employed. To control the depth of the hole, the drill rod was marked with the length of the desired depth. Drilling continued until the bit moved into the sample up to the marked position. Recording of the interferograms commenced immediately after the drilling was completed (as in Fig. 2) to document the influence of thermal diffusion on the shape of the interferograms. From the numerical model we know the shape of the final stress-relief interferograms to be expected from each experimental configuration. The shapes of the fringe patterns were monitored until an expected fringe pattern stabilized, at which point we took the stress measurement. This was typically about 30 min after drilling had ceased. While the experiment progressed, the stress on the sample was also continually monitored and maintained at a constant level according to the response of a calibrated load cell.

In the different tests, experimental conditions were varied by changing the stress level or by changing the direction of the uniaxial stress axis with respect to the $S1$ and $S2$. In the present study, two geometries were tested, one for the situations where the line joining the sources and uniaxial stress axis are parallel (i.e. $S1$ and

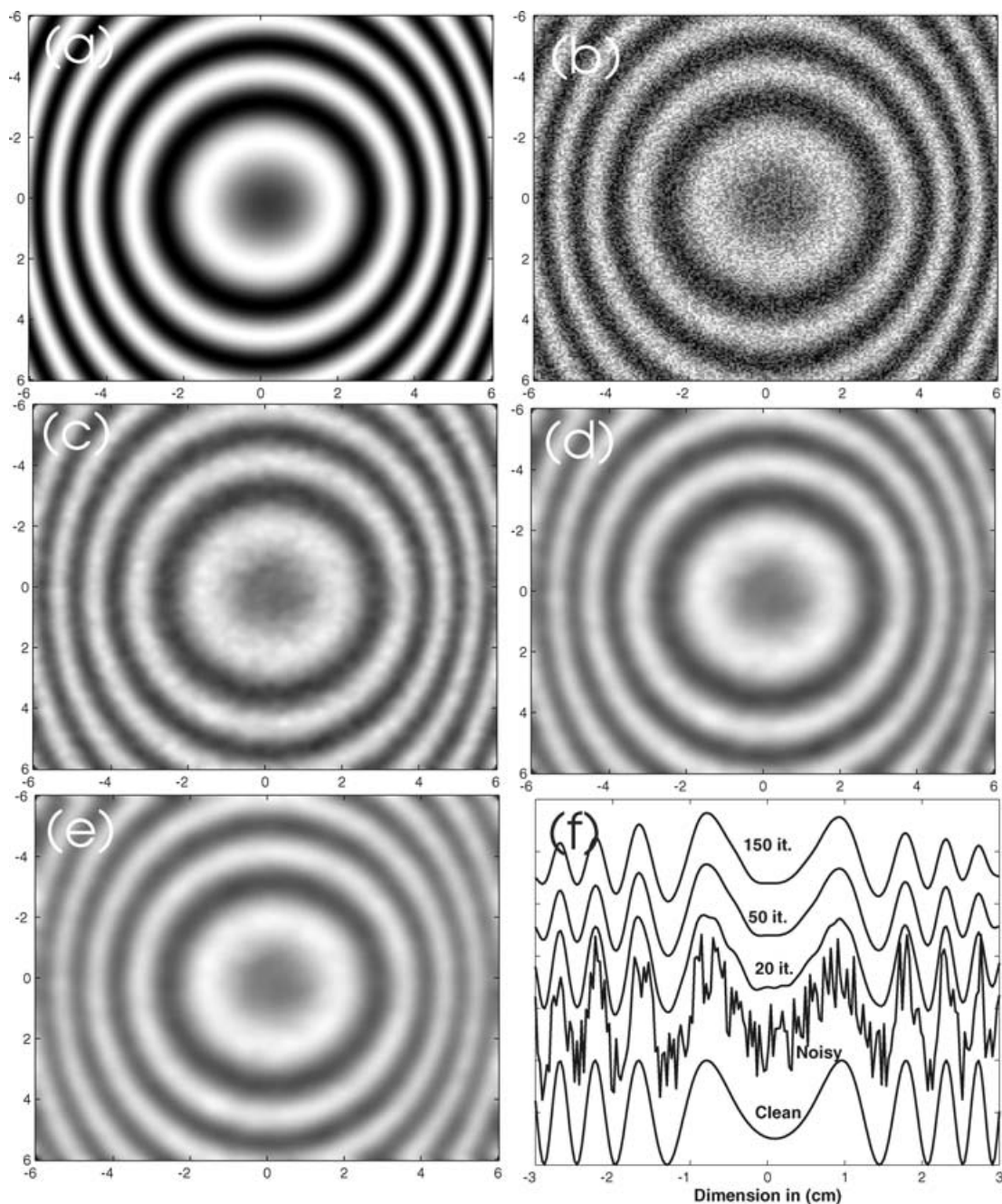


Figure 9. Comparison of noisy calculated fringes before and after application of the mean curvature diffusion smoothing technique. The model consists of a $7\ \mu\text{m}$ translation (a) Clean fringes, (b) Noisy fringes. Filtered fringes after (c) 20 iterations, (d) 50 iterations, (e) 150 iterations. (f) Line plot comparisons of the clean, noisy, and filtered profile passing through the centre of the original image.

S_2 are collinear with the direction of σ_{xx} and the other where the plane containing the sources is perpendicular to the stress axis (i.e. S_1 and S_2 are perpendicular with the direction of σ_{yy}). Again, Fig. 2 shows two illustrative examples of raw interferograms. Those in the left column [Figs 2a(1–3)] were obtained with a uniaxial stress of approximately 4.0 MPa applied along the X direction, and those in the right column [Figs 2b(1–3)] were obtained with a uniaxial stress of 5.4 MPa along the Y direction. In each experiment, speckle patterns were acquired for many hours after drilling to make sure that elastic relaxation part of the stress-relief process was captured (Schmitt & Hunt 1999). The first interferogram of the left column (Fig. 2a-1) was obtained approximately 30 min after drilling. Most

of the heat of drilling had dissipated by this time and the subsequent fringe patterns Fig. 2(a-2) and Fig. 2(a-3) taken 196 min and 394 min, respectively, after drilling show little further change. In contrast, the first interferogram the second sequence of the right column (Fig. 2b-1) was acquired immediately (within 1 min) after the drilling operation and shows a complex fringe pattern related to the thermal expansion of heat generated at the wall of the stress-relief hole by friction with the drill bit. The latter fringe patterns [Fig. 2b(2–3)] are largely stable with only small variations seen between these two frames taken 161 min apart from each other.

The fringe picking is carried as follows. First we select a point around the region where we expect to find the fringe extrema. Then

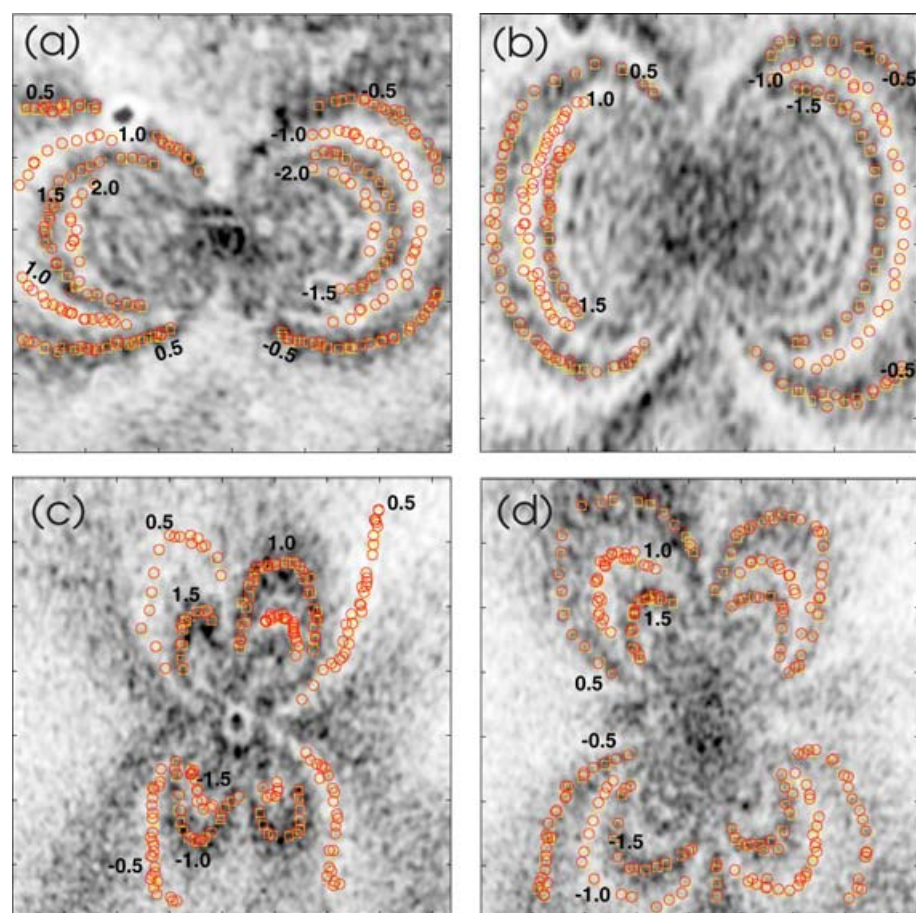


Figure 10. Picked real fringe patterns from the four analysed samples (Table 1) subject to uniaxial stress states of. (a) Test 1: $\sigma_{xx} = 5.5$ MPa, (b) Test 2: $\sigma_{xx} = 4.06$ MPa, (c) Test 3: $\sigma_{yy} = 3.8$ MPa, and (d) Test 4: $\sigma_{yy} = 5.4$ MPa.

we search for an extremum in this region delimited by a square patch around the initial guess. The size of this square in pixels determines the extent of the region to be used for this extremum search. In Fig. 10 we show the real interferograms from the four samples after MCD smoothing, superimposed with the initial (open circle) and the finally determined (open square) fringe extrema.

Although only uniaxial stresses were applied to the blocks, a full biaxial inversion was done in order to assess the level of errors that might be introduced in an actual analysis of the data.

RESULTS AND DISCUSSION

The four fringe patterns analysed are shown in Fig. 10 with the corresponding experimental conditions and the final results of the fringe pattern inversions provided in Table 1. Some important observations from these images are:

(i) Although the uniaxial stresses applied have similar magnitudes, the fringe patterns observed have completely differently shapes. For example, the bow-tie pattern of Fig. 2a-3 differs from the butterfly pattern of Fig. 2b-3. This is entirely due to the geometry of the optical configuration relative to the applied stresses.

(ii) These real fringe patterns of Figs 2 and 7(c) lack the resolution apparent in the synthetic fringe pattern of Fig. 7(d). This is due to pixel resolution of the camera and made worse by the local correlation technique used in calculating the fringe pattern.

(iii) Time-dependent effects are important in such drilling tests. In both cases, a considerable amount of time is required (at least 30 min) for thermal expansion due to drill heating to decay in order to observe the stress-relief displacements. This complicates the interpretation of the fringe patterns for two reasons. First, it may be difficult to know how long is required for the transient thermal effects to satisfactorily dissipate in order that the fringe pattern contains primarily stress-relief information. Second, the longer the waiting period before the stress-relief pattern is taken the greater the potential that the final fringe pattern may be contaminated by translational displacements of the optical system itself or by time-dependent inelastic deformation of the rock mass. This is evident in the changes to the inverted stress values (Fig. 11) particularly at long times.

The fringe analysis and inversion procedures described above yielded inverted stress values shown in Table 1. The inverted uniaxial stress values differ from those actually applied from 3.7 to 37 per cent with a mean value of 19 per cent for the four measurements. The full inversion procedure also yields values of the two other biaxial stress components that are not applied to the real sample. Some of these errors are greater than, but comparable to, those recently found in a series of tests on alloys. (Steinzig & Takahashi 2003).

These observed errors are significant, particularly when compared to the results of an extensive series of synthetic tests on forward

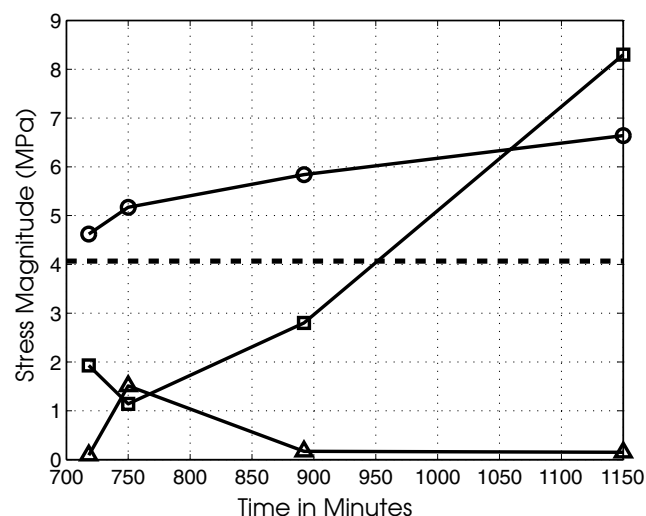


Figure 11. Inverted stresses versus measurement time for Test 2 with $\sigma = [4.07 \ 0 \ 0]$ of σ_{xx} (open circles), σ_{yy} (open squares), and τ_{xy} (open triangles) to highlight the effects of time-dependent deformation.

modelled fringe patterns with a variety of different kinds of noise added that suggested an uncertainty of 3 per cent was achievable, (Diaz *et al.* 2001). Low levels of experimental error (~ 4 per cent) were also found in a similar inversion procedure applied to a elastic moduli determination on this same acrylic (Shareef & Schmitt 2004). This low level of error was not obtained in the current test. There are a number of reasons for these errors (Schmitt & Hunt 1999) including uncertainties in the relative positioning of the various optical components and the sample, uncertainty in the values of the elastic moduli used, the loss of imaging resolution due to the speckle and fringe calculation, the existence of thermal, translational, and inelastic deformations, and the possibility of decorrelation effects near the stress-relieving hole.

The inversion method here appears to work well although the manual picking of fringe loci and semi-manual interpretation of fringe order is awkward. These restrictions would make the method impractical under field conditions where a rapid solution is required. Future work must examine alternative methods of extracting this information and here some of the recent developments associated with the analysis of INSAR data may be informative. Fukushima *et al.* (2005) developed a Monte Carlo inversion based on Sambridge's neighbourhood search algorithm (1999a, 1999b) and a novel mixed boundary element method to tie geometry, stress, and elastic moduli to surface displacements (Cayol & Cornet 1997). Such a technique, or similar genetic or simulated annealing methods, may allow direct analysis of the entire fringe pattern, not just the limited number of points that were manually picked.

The capability of imaging the time-dependent displacement field is highly useful as it is doubtful that the thermal effects would be as readily detected using standard strain gage techniques. While having this data is certainly advantageous, one must be careful in using this extra information. In particular, it is difficult to know exactly the point at which one should make the measurement. Depending on the material, one may have to balance decay of the overwhelming early thermal signal against more time-dependent plastic or viscoelastic motions if a proper stress measurement is to be made. Indeed, it is useful to track how the inverted stresses may change with time in a sample that is subject to inelastic deformations. In a material subject to time-dependent deformation, one will expect the inelastic

Table 2. Comparison of thermal properties of differing materials.

Material	Aluminium alloy	PMMA	Rock
Thermal conductivity ($\text{W m}^{-1} \text{K}$)	238	0.21	1–4
Mass density (kg m^{-3})	2700	1190	2000–3000
Heat capacity ($\text{J kg}^{-1} \text{K}$)	917	1470	700–1000
Thermal diffusivity ($\text{m}^2 \text{s}^{-1}$) $\times 10^7$	960	1.2	3.3–28.6
Relative thermal time (reference to Aluminium)	1	28	17–5.8

deformations to continue and to be superimposed on the instantaneous elastic motions. It is useful to see how this might influence the measured stresses; the variation in the apparent stress with time is due to such motions in the PMMA (Fig. 11) and, as a result, it is important that all thermal disturbances have decayed prior to making the final measurement. We note that other stress-relief techniques in rock will be subject to similar limitations but we are not aware of such factors being accounted for in earlier works.

Nearly all blind hole drilling tests previously described in the literature have been made on aluminium alloys or steel; and most of the analytic techniques focus on a narrow range of problems devoted to such materials. Aside from the strength and elastic modulus, the acrylic differs significantly in terms of its ability to conduct heat. The thermal diffusivity:

$$\kappa = \frac{k}{\rho C_p}, \quad (11)$$

where k is the thermal conductivity, ρ is the mass density, and C_p is the heat capacity, is a useful measure of how long it will take heat to move within a material. A crude estimate of the relative time it would take to obtain the same degree of cooling in different materials this is given by $\sqrt{\kappa_1/\kappa_2}$. The times relative to that for aluminium are also given in Table 2 and indicate that the transient thermal response of the low-diffusivity acrylic requires nearly 30 times longer for heat to decay than in aluminium. It is interesting to compare these results to rock where a broad range of different properties show that most rocks will also require a substantial cooling time. Thus, the use of the acrylic is a useful analogue to rock with regards to the dissipation of heat.

CONCLUSION

The results of the calibration tests described above indicate that the ESPI stress-relief technique shows promise but that more work is required to bring the technique to the level required for accurate quantitative measurements. Some technical improvements to the current technique will require more reliable methods for positioning of the optical system relative to the object of study and in extracting the relevant low-frequency fringe information. The current inversion procedure of picking the bright and dark fringes uses only a small fraction of all the information contained in the fringe pattern; inclusion of the grey-scale values via a phase unwrapping or other inversion technique would provide a much better statistical answer. Future work will include refinement of these techniques as well as application to rock samples. Towards this end, a more compact and rugged ESPI camera has been constructed and tested.

Although the current tests focused on acrylic, the ultimate goal of the research will be to use the method to measure rock stress from a

wellbore. Ideally, the potential advantage of such optical techniques are that the *in situ* stress at a given depth along the wellbore could be obtained rapidly and with minimal disturbance as first tested by Bass *et al.* (1986). The static elastic moduli are also necessary and a complementary optical method allows them to be measured over similar dimensions and displacement magnitudes (Shareef & Schmitt 2004). One may be able to obtain the entire stress tensor: both directions and magnitudes.

However, all stress determination methods currently employed are in some way limited in the situations to which they may be applied. All the techniques, including this optical method, rely on numerous assumptions about the rock mass. A particular limitation of the interferometric method at this current stage of development is that it assumes the rock to be linearly elastic and isotropic. Thus, the method will have limited success in wellbores in which the rock is close to failure such that the concentrations of the far-field stresses by the wellbore cavity will already have been relieved. It is now well understood that most rocks are anisotropic due to their intrinsic structure and to anisotropic stresses. This problem may be particularly frustrating in borehole measurements where azimuthally varying stress concentrations produced azimuthally varying elastic properties (Schmitt 1987; Winkler 1996). As a result, it will be important to include more appropriate constitutive relations in future work possibly requiring non-linear elasticity and even time-dependent viscoelastic responses. It must be noted that use of such relations is still at an immature stage with regards to the field of rock mechanics as a whole. The grain sizes will also be a limitation as in many rocks the stress state is likely non-uniform on the granular scale due to various stress concentrations between minerals and pores. The stress-relief technique will be sensitive to these heterogeneities. The role of residual stresses within the rock are poorly understood (Engelddger 1993); stress-relief techniques cannot separate applied from residual stresses, which could be a source of error in measurements. However, with continued development, the method may allow us to better understand these often ignored residual stresses.

On a final note, although this contribution has focused on developments towards a quantitative stress-measurement technique, recent technical developments in inexpensive diode lasers, and image processing, acquisition hardware, and software has made such techniques readily accessible to the geoscience community. One can envisage extensions of this method to shorter timescales in the study of complex wave (e.g. van Wijk *et al.* 2005) and fracture propagation (Xia *et al.* 2005) problems and may provide methods to complement geological analogue studies that use recently developed particle imaging velocimetry (e.g. Adam *et al.* 2005). The direct comparison of this method to satellite borne radar interferometry is obvious, and use of the method to temporally track surface motions in laboratory physical modelling experiments can likely add insight into the deformations resulting from tectonic straining of complex geological structures: deformations that still remain difficult to compute using the most advanced numerical methods.

ACKNOWLEDGMENTS

L. Tober assisted in the preparation of the experimental set up. W. Engler developed the image acquisition and fringe calculation programs. The encouragement of D. Kenway is greatly appreciated. This work was funded by the NSERC Strategic Grant and Canada Research Chair Programs of DRS. The authors thank the two

reviewers and the editors for their conscientious efforts towards improving this manuscript.

REFERENCES

- Adams, L.H. & Williamson, E.D., 1923, On the compressibility of minerals and rocks at high pressures, *J. Franklin Inst.*, **195**, 475–529.
- Adam, J. *et al.*, 2005. Shear localisation and strain distribution during tectonic faulting—new insights from granular-flow experiments and high-resolution optical image correlation techniques, *J. Struct. Geol.*, **27**, 283–301.
- Amadei, B. & Stephannson, O., 1997. *Rock Stress and Its Measurement*, Kluwer Academic Publishers, Boston, MA, p. 512.
- American Society for Testing and Materials, Standard Test Method for Determining Residual Stresses by the Hole Drilling Strain-gage Method, *ASTM*, 2001, E837–99, Philadelphia, PA, pp. 675–684.
- Bass, J.D., Schmitt, D.R. & Ahrens, T.J., 1986. Holographic *in situ* stress measurements, *Geophys. J. R. astr. Soc.*, **85**, 14–41.
- Beghini, M. & Bertini, L., 2000. Analytical expressions of the influence functions for accuracy and versatility improvement in the hole-drilling method, *Journal Strain Analysis*, **35**(2), 125–135.
- Biolzi, L., Cattaneo, S. & Rosati, G., 2001. Flexural/tensile strength ratio in rock-like materials, *Rock Mechanics Rock Engineering*, **34**, 217–233.
- Boness, N.L. & Zoback, M.D., 2004, Stress-induced velocity anisotropy and physical properties in the SAFOD pilot hole in Parkfield, CA, *Geophys. Res. Lett.*, **31**, Art. No. L15S17.
- Cayol, V. & Cornet, F.H., 1997. 3D mixed boundary elements for elastostatic deformation fields analysis, *International Journal Rock Mechanics Mineral Science Geomechanics Abstract*, **34**, 275–287.
- Cloud, G., 1995. *Optical Methods in Engineering Analysis*, Cambridge University Press, New York, p. 517.
- Diallo, M. & Schmitt, D.R., 2004. Noise reduction in interferometric fringe patterns with mean curvature diffusion, *Journal of Electronic Imaging*, **13**, 819–831.
- Diaz, F.V., Kaufmann, G.H. & Möller, O., 2001. Residual stress determination using blind-hole drilling and digital speckle pattern interferometry with automated data processing, *Experimental Mechanics*, **41**, 319–323.
- Engelddger, T., 1993. *Stress Regimes in the Lithosphere*, Princeton University Press, Princeton, New Jersey, p. 457.
- Engler, W., 2002. Laser speckle interferometry: A stochastic investigation, *M.Sc. Thesis*, Department of Physics, University of Alberta.
- Fairhurst, C., 2003. Stress estimation in rock: a brief history and review, *International Journal Rock Mechanics and Minerals Science*, **40**, 957–973.
- Focht, G. & Schiffner, K., 2003. Determination of residual stresses by an optical correlative hole-drilling method, *Experimental Mechanics*, **43**, 97–104.
- Fukushima, Y., Cayol, V. & Durand, P., 2005. Finding realistic dike models from interferometric synthetic aperture radar data: the February 2000 eruption at Piton de la Fournaise, *J. geophys. Res.*, **110**, B03206, doi:10.1029/2004JB003268.
- Furguele, F.M., Pagnotta, L. & Poggialini, A., 1991. Measuring residual stresses by hole-drilling and coherent optics techniques: a numerical calibration, *ASME Journal Engineering Material and Technology*, **113**, 41–50.
- Ghiglia, D.C. & Pritt, M.D., 1998. *Two-dimensional Phase Unwrapping Theory, Algorithms, and Software*, Wiley, New York.
- Hiramatsu, Y. & Oka, Y., 1962. Stress around a shaft or level excavated in ground with a three-dimensional stress state, *Mem. Fac. Eng. Kyoto Univ.*, **24**, 56–76.
- Jones, R. & Wykes, C., 1989. *Holographic and speckle interferometry*, 2nd edn, Cambridge University Press, Cambridge, UK, p. 368.
- Kaselow, A. & Shapiro, S.A., 2004. Stress sensitivity of elastic moduli and electrical resistivity in porous rocks, *J. Geophys. asnd Eng.*, **1**, 1–11.

- Ljunggren, C., Yanting Chang, T., Janson, T. & Christiansson, R., 2003. An overview of rock stress measurement methods, *International Journal Rock Mechanics and Minerals Sci.*, **40**, 975–989.
- Maji, A.K. & Wang, J.L., 1992. Experimental-study of fracture processes in rock, *Rock Mechanics and Rock Eng.*, **25**, 25–47.
- Makino, A., Nelson, D.V., Fuchs, E.A. & Williams, D.R., 1996. Determination of biaxial residual stresses by holographic-hole drilling technique, *Journal Engineering Material & Technology*, **119**, 583–588.
- Massonnet, D. & Feigl, K.L., 1998. Radar interferometry and its application to changes in the earth's surface, *Rev. Geophys.*, **36**, 441–500.
- McDonach, A., McKelvie, J., MacKenzie, P. & Walker, C.A., 1983. Improved Moiré interferometry and applications in fracture mechanics, residual stresses, and damaged composites, *Experimental Technology*, **7**, 20–24.
- Mizutani, H. & Takemoto, S., 1989. Application of holographic interferometry to underground stress measurements, in *Laser Holography in Geophysics*, pp. 106–128, ed. Takemoto, S., Ellis Horwood Series in Applied Geology, John Wiley and Sons, New York.
- Nelson, D.V. & McCrickerd, J.T., 1986. Residual stress measurement through combined use of holographic interferometry and blind hold drilling, *Exp. Mech.*, **26**, 371–378.
- Nelson, D.V., Makino, A. & Schmidt, T., 2006. Residual stress determination using hole drilling and 3D image correlation, *Exp. Mech.*, **46**, 31–38.
- Park, D.W. & Jung, J.O., 1988. Application of holographic-interferometry to the study of time-dependent behavior of rock and coal, *Rock Mechanics Rock Engineering*, **21**, 259–270.
- Ponslet, E. & Steinzig, M., 2003. Residual stress measurement using the hole drilling method and laser speckle interferometry Part II: analysis technique, *Experimental Techniques*, **27**, 17–21.
- Rendler, N.J. & Vigness, I., 1966. Hole-drilling strain-gage method of measuring residual stresses, *Experimental Mechanics*, **21**, 577–586.
- Rumzan, I. & Schmitt, D.R., 2003. Three-dimensional stress-relief displacements from blind-hole drilling: a parametric description, *Experimental Mechanics*, **43**, 52–60.
- Sambridge, M., 1999a. Geophysical inversion with a neighbourhood algorithm—I. Searching a parameter space, *Geophys. J. Int.*, **138**, pp 479–494.
- Sambridge, M., 1999b. Geophysical inversion with a neighbourhood algorithm—II. Appraising the ensemble, *Geophys. J. Int.*, **138**, 727–746.
- Schajer, G.S., 1981. Application of Finite Element Calculations to Residual Stress Measurements, *Journal Engineering Material Technology*, **103**, 157–163.
- Schmitt, D.R., 1987. I. Application of double exposure holography to the measurement of in situ stress and the elastic moduli of rock from boreholes, II. Shock temperatures in fused quartz and crystalline NaCl to 35 GPa, *PhD thesis*, California Institute of Technology, Pasadena, California, 170 pp.
- Schmitt, D.R. & Hunt, R.W., 1997. Optimization of fringe pattern calculation using direct correlation in speckle interferometry, *Applied Optics*, **36**, 8848–8857.
- Schmitt, D.R. & Hunt, R.W., 1999. Time-lapse speckle interferometry, *Geophys. Res. Lett.*, **26**, 2589–2592.
- Schmitt, D.R. & Hunt, R.W., 2000. Inversion of speckle interferometer fringes for hole-drilling residual stress determinations, *Experimental Mechanics*, **40**, 129–137.
- Schmitt, D.R. & Li, Y., 1996. Three Dimensional Stress Relief Displacements from Drilling a Blind Hole, *Experimental Mechanics*, **36**, 412–420.
- Schmitt, D.R., Smither, C.L. & Ahrens, T.J., 1989. In situ holographic elastic moduli measurements from boreholes, *Geophysics*, **54**, 468–477.
- Schwarz, R.C., Kutt, L.M., Papazin, J.M., 2000. Measurement of residual stress using interferometric Moiré: A new insight, *Experimental Mechanics*, **40**, 217–281.
- Shareef, S. & Schmitt, D.R., 2004. Point load determination of static elastic moduli using laser speckle interferometry, *Optics and Lasers in Engineering*, **42**, 511–527.
- Smither, C.L., Schmitt, D.R. & Ahrens, T.J., 1989. Analysis and modelling of holographic measurements of in situ stress, *International Journal Rock Mechanics Mining Science & Geomechanics, Abstract*, **25**, 353–369.
- Spetzler, H., Scholz, C.H., Lu, C.H. & Ti, C.P.J., 1974. Strain and creep measurements on rocks by holographic interferometry, *Pure appl. Geophys.*, **112**, 571–581.
- Spetzler, H., Sobolev, G.A., Sondergeld, C.H., Salov, B.G., Getting, I.C. & Koltsov, A., 1981. Surface deformation, crack formation, and acoustic velocity changes in pyrophyllite under polyaxial loading, *J. geophys. Res.*, **86**, 1070–1080.
- Steinzig, M. & Takahashi, T., 2003. Residual stress measurement using the hole drilling method and laser speckle interferometry Part IV: Measurement accuracy, *Experimental Technology*, **27**, 59–63.
- Takemoto, S., 1986. Application of laser holographic techniques to investigate crustal deformations, *Nature*, **322**, 49–51.
- Takemoto, S., 1989. *Laser Holography in Geophysics, Ellis Horwood Series in Applied Geology*, John Wiley and Sons, New York.
- Takemoto, S., 1990. Real time holographic measurements of tidal deformation of a tunnel, *Geophys. J. Int.*, **100**, 99–106.
- Takemoto, S., 1996. Holography and electronic speckle pattern interferometry in geophysics, *Optics and Lasers in Engineering*, **24**, 145–160.
- Takemoto, S. *et al.*, 2004. 100 m laser strainmeter system installed in a 1 km deep tunnel at Kamioka, Gifu, Japan, *J. Geodyn.*, **38**, 477–488.
- van Wijk, K., Scales, J.A., Mikesell, T.D. & Peacock, J.R., 2005. Toward noncontacting seismology, *Geophys. Res. Lett.*, **32**, Art. No. L01308.
- Vikram, C.S., Perchersky, M.J., Feng, C. & Engelhaupt, D., 1995. Residual stress analysis by local laser heating and speckle-correlation interferometry, *Experimental Technology*, **34**, 2964–2971.
- Wang, C.Y., Liu, P.D., Hu, R.S. & Sun, X.T., 1990. Study of the fracture process zone in rock by laser speckle interferometry, *International Journal Rock Mechanics Mineral Science & Geomechanics Abstract*, **27**, 65–69.
- Whiters, P.J. & Badheshia, H.K.D.H., 2001. Residual stress part 1—measurement techniques, *Mat. Sci. and Tech.*, **71**, 355–365.
- Winkler, K.W., 1996. Azimuthal velocity variations caused by borehole stress concentrations, *Journal of Geophysical Research Solid Earth*, **101**, 8615–8621.
- Xia, K.W., Rosakis, A.J., Kanamori, H. & Rice, J., 2005. Laboratory earthquakes along inhomogeneous faults: Directionality and supershear, *Science* **308** 681–684.
- Zhang, J., 1998. Two-dimensional in-plane electronic speckle pattern interferometer and its application to residual stress determination, *Optical Engineering*, **37**, 2402–2409.